

Breakdown of the Law of Reflection at a Disordered Graphene Edge

E. Walter,^{1,2,*} T. Ö. Rosdahl,^{3,†} A. R. Akhmerov,³ and F. Hassler¹

¹JARA Institute for Quantum Information, RWTH Aachen University, 52056 Aachen, Germany

²Arnold Sommerfeld Center for Theoretical Physics,

Ludwig-Maximilians-University Munich, 80333 Munich, Germany

³Kavli Institute of Nanoscience, Delft University of Technology, P.O. Box 4056, 2600 GA Delft, Netherlands

(Dated: August 24, 2018)

The law of reflection states that smooth surfaces reflect waves specularly, thereby acting as a mirror. This law is insensitive to disorder as long as its length scale is smaller than the wavelength. Monolayer graphene exhibits a linear dispersion at low energies and consequently a diverging Fermi wavelength. We present proof that for a disordered graphene boundary, resonant scattering off disordered edge modes results in diffusive electron reflection even when the electron wavelength is much longer than the disorder correlation length. Using numerical quantum transport simulations, we demonstrate that this phenomenon can be observed as a nonlocal conductance dip in a magnetic focusing experiment.

Introduction.—The law of reflection is a basic physical phenomenon in geometric optics. As long as the surface of a mirror is flat on the scale of the wavelength, a mirror reflects incoming waves specularly. In the opposite limit when the surface is rough, reflection is diffusive and an incident wave scatters into a combination of many reflected waves with different angles. This picture applies to all kinds of wave reflection, including sound waves and particle waves in quantum systems. The phenomenon has been extensively investigated both theoretically and experimentally in the past, e.g., in order to understand sea clutter in radar [1] as well as a method to measure surface roughness [2].

Graphene [3, 4] is a gapless semiconductor with a linear dispersion relation near the charge neutrality point, and therefore a diverging Fermi wavelength. Modern techniques allow for the creation of graphene monolayers of high mobility, with mean free paths of tens of microns [5–8]. This makes it possible to realize devices in which carriers propagate ballistically over mesoscopic distances, facilitating the design of electron optics experiments [9–11]. For example, recent experiments employ perpendicular magnetic fields to demonstrate snaking trajectories in graphene p - n junctions [12, 13], or the magnetic focusing of carriers through cyclotron motion [14]. The latter tests the classical skipping orbit picture of carrier propagation along a boundary [15], and using a collimator to focus a narrow beam of electrons with a small angular spread enhances the focusing resolution [16]. The high mobility in the bulk together with a large Fermi wavelength suggest that graphene is a promising medium for the design of advanced electron optics and testing the law of reflection, cf. Fig. 1.

Graphene edges are rough due to imperfect lattice termination or hydrogen passivation of dangling bonds [17, 18]. Boundary roughness may adversely affect device performance [19–22]. On the other hand, close to the charge neutrality point the Fermi wavelength in graphene diverges, and by analogy with optics, one may expect that

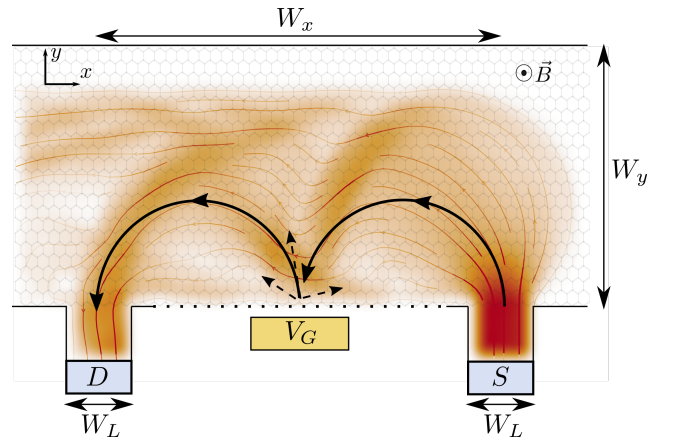


FIG. 1. Sketch of the setup. Electrons injected at the source (S) follow cyclotron trajectories due to the perpendicular magnetic field $\mathbf{B} = B\hat{z}$, forming a hot spot at the boundary where most trajectories scatter. If the trajectories specularly reflect at the boundary and the separation W_x between the midpoints of the source and the drain (D) matches two cyclotron diameters, most trajectories enter the drain, and a focusing peak manifests in the nonlocal conductance. The focusing is evident in the classical cyclotron trajectory of an electron normally incident from S at the Fermi level (solid curves), and in the computed current distribution that is superimposed on the device (flow lines, colored background). A side gate V_G controls the average potential at the disordered boundary (dotted line), and allows us to tune between regimes of specular and diffusive reflection (see main text). In the diffusive regime, electrons scatter into random angles as shown schematically with the dashed lines, resulting in a drop in the focusing peak conductance compared to the regime of specular reflection. The graphene sheet is grounded, such that current due to off-resonance trajectories may drain away to the sides (open boundaries).

the law of reflection holds and suppresses the diffusive boundary scattering.

In this Letter, we study how the microscopic boundary properties influence electron reflection off a graphene

boundary. Most boundaries result in the self-averaging of the boundary disorder, and therefore obey the law of reflection. However, we find that, due to resonant scattering, electrons are reflected diffusively regardless of the Fermi wavelength when the disorder-broadened edge states overlap with $E = 0$. As a result, in this situation, the boundary of graphene never acts as a mirror and thus breaks the law of reflection. We demonstrate that this phenomenon can be observed as a dip in the nonlocal conductance in a magnetic focusing setup (see Fig. 1). We confirm our predictions by numerical simulations.

Reflection at a disordered boundary.—To demonstrate the breakdown of the law of reflection, we first analyze scattering at the edge of a semi-infinite graphene sheet. We consider a zigzag edge, since the zigzag boundary condition applies to generic lattice terminations [23]. To begin with, we neglect intervalley scattering to simplify the analytical derivation, and focus on the single valley Dirac Hamiltonian

$$H = v_F \boldsymbol{\sigma} \cdot \mathbf{p}, \quad (1)$$

with v_F the Fermi velocity, $\boldsymbol{\sigma} = (\sigma_x, \sigma_y)^T$ the vector of Pauli matrices in the (sublattice) pseudospin space, and \mathbf{p} the momentum. We later verify the validity of our conclusions with tight-binding calculations that include intervalley scattering. We introduce edge disorder by randomly sampling the most general single-valley boundary condition [23–25] over the edge, such that the boundary condition for the wave function reads

$$\psi(x, y = 0) = [\cos \theta(x) \sigma_z + \sin \theta(x) \sigma_x] \psi(x, y = 0), \quad (2)$$

where disorder enters through the position-dependent parameter θ , and $\theta = 0$ gives a zigzag segment. We take $\theta(x)$ to follow a Gaussian distribution with mean value $E[\theta(x)] = \theta_0$ and covariance $\text{Cov}[\theta(x), \theta(x')] = s_\theta^2 e^{-\pi(x-x')^2/d^2}$, with d the correlation length. In this work, $E[A]$ is the statistical average of A over the disordered boundary, and the corresponding variance $\text{Var}(A)$. The boundary condition (2) applies to different microscopic origins of disorder, such as hydrogen passivation of dangling bonds [23] or edge reconstruction [26].

To solve the scattering problem, we introduce periodic boundary conditions parallel to the boundary with period L , such that the momentum $k_\parallel \in \{2\pi n/L \mid n \in \mathbb{Z}\}$ is conserved. At the Fermi energy E_F , the disordered boundary scatters an incident mode $\psi_{k_\parallel}^{\text{in}}$ into the outgoing modes $\psi_{k'_\parallel}^{\text{out}}$. The scattering state is

$$\psi_{k_\parallel} = \psi_{k_\parallel}^{\text{in}} + \sum_{k'_\parallel} \psi_{k'_\parallel}^{\text{out}} S_{k'_\parallel k_\parallel}, \quad (3)$$

where modes with $k_\parallel > k_F$ are evanescent but others propagating, with k_F the Fermi momentum, and $S_{k'_\parallel k_\parallel}$ the reflection amplitudes. An outgoing propagating mode moves

away from the edge at the angle $\varphi_{k_\parallel} = \arctan(v_\parallel/v_\perp)$ relative to the boundary normal, with v_\parallel and v_\perp the velocities along and perpendicular to the boundary. For the incident propagating mode at k_\parallel , the quantum mechanical average reflection angle is therefore

$$\langle \varphi_{k_\parallel} \rangle = \sum_{k'_\parallel} \varphi_{k'_\parallel} |S_{k'_\parallel k_\parallel}|^2, \quad (4)$$

where the sum is limited to propagating modes, and $|S_{k'_\parallel k_\parallel}|^2$ is the reflection probability into the outgoing mode at k'_\parallel . An incident mode reflects specularly if $S_{k'_\parallel k_\parallel} = \delta_{k'_\parallel k_\parallel}$, but diffusively if it scatters into multiple angles, and the variance $\sigma^2(\varphi_{k_\parallel})$ is therefore finite for the latter. If N modes are incident, diffusiveness manifests in a finite mode-averaged variance $\sigma^2(\varphi) = \sum_{k_\parallel} \sigma^2(\varphi_{k_\parallel})/N$, or its statistical average $E[\sigma^2(\varphi)]$ over the disordered boundary. If $\lambda_F \ll L$, then $\sigma^2(\varphi)$ automatically includes the statistical average $E[\sigma^2(\varphi)]$, because the incident waves sample multiple different segments of the boundary within each period.

The scattering problem simplifies at the charge neutrality point $E_F = 0$, where only two propagating modes are active, one incident and one outgoing, both with $k_\parallel = 0$. The scattering matrix relating the propagating modes is therefore a phase factor $e^{i\phi}$, with ϕ the scattering phase, and the quantum mechanical averages of the preceding paragraph are not necessary. We expect diffusiveness to manifest as a finite variance $\text{Var}(\phi)$, and have verified this numerically. To compute ϕ , we impose the boundary condition (2) on the scattering state (3).

If θ_0 is nonzero and $s_\theta \ll \theta_0$, ϕ follows a Gaussian distribution [27] with the mean

$$E[\phi] \stackrel{L \gg d}{=} -\theta_0 + \frac{s_\theta^2}{2 \sin(\theta_0)} + \mathcal{O}\left(\frac{s_\theta^3}{\theta_0^3}\right) \quad (5)$$

and variance

$$\text{Var}(\phi) = \frac{d}{L} s_\theta^2 + \mathcal{O}\left(\frac{s_\theta^3}{\theta_0^3}\right). \quad (6)$$

Thus $E[\phi]$ is given by θ_0 , with the addition of a random walklike drift term proportional to s_θ^2 . In addition, $\text{Var}(\phi)$ increases with s_θ^2 , but increasing the boundary length suppresses it as $1/L$. In the limit $L \rightarrow \infty$ reflection is thus completely specular, with a fixed scattering phase ϕ . This algebraic decay of diffusive scattering resembles a classical optical mirror [2].

If $\theta_0 = 0$, surprisingly there is no suppression of $\text{Var}(\phi)$ with L . Rather, we find [27] that $\tan \phi$ follows a Cauchy distribution $f(\tan \phi) = \gamma/\pi(\tan^2 \phi + \gamma^2)$ with $E[\phi] = 0$, $\text{Var}(\phi) \approx 2.2 s_\theta$ linear in s_θ instead of quadratic, and $\gamma \approx 0.8 s_\theta$ obtained numerically. In this case, the law of reflection therefore breaks down and scattering is always diffusive. The distribution of the scattering phase follows

the Cauchy distribution also when the disorder is non-Gaussian and even asymmetric, as long as θ_0 is sufficiently small. For an asymmetric distribution, the value of γ/s_θ weakly depends on higher cumulants of the distribution of $\theta(x)$.

Generic graphene boundaries support bands of edge states with a linear dispersion [23, 26]. Because the matrix element between the edge state and the edge disorder is inversely proportional to the spatial extent of the edge state, the disorder broadening of these edge states is proportional to the momentum along the boundary [see Figs. 2(c), 2(d)]. In other words linearly dispersing edge states turn into disorder-broadened bands with both the average velocity and the bandwidth proportional to k_\parallel . When these bands overlap with $E = 0$ they serve as a source of resonant scattering responsible for the breakdown of the law of reflection. Indeed, we find that the condition for diffusive scattering occurs for any $\theta_0 \lesssim s_\theta$.

To include intervalley scattering, we compute the scattering phase at the charge neutrality point using the nearest neighbor tight-binding model of graphene, with random on-site disorder in the outermost row of atoms taken from a Gaussian distribution with mean V_d and variance s_d^2 [27]. The results, shown in Fig. 2(b), agree with the single valley prediction of the Dirac equation up to numerical prefactors.

To extend our analysis to nonzero E_F , we employ the tight-binding model with on-site disorder to study the reflection angle φ at the disordered boundary numerically using Kwant [28]. The disordered edge band now resides at the energy V_d , as Figs. 2(c) and 2(d) show. Figures 2(a), 2(b) confirm that $\sigma^2(\varphi) \approx \text{Var}(\phi)$ at $E = 0$. The law of reflection is broken for all s_d at $V_d = E_F$ and $\text{Var}(\phi)$ increases linearly with s_d , independent of λ_F . Further, the reflection becomes specular for $s_d \lesssim |V_d - E_F|$. As Fig. 2(b) shows, $\text{Var}(\phi)$ [$\sigma^2(\varphi)$] increases quadratically with the disorder strength s_d , but decays as $1/L$ [$1/\lambda_F$] (Fig. 2(a)) when the Fermi wavelength becomes large compared to the lattice constant a , such that scattering is predominantly specular. However, for $s_d \gtrsim |V_d - E_F|$ reflection becomes diffusive, and moving V_d closer to E_F [Fig. 2(b)] shifts the transition from specular to diffusive reflection to smaller s_d .

Experimental detection.—Any experiment that is sensitive to the microscopic properties of a disordered boundary will detect the breakdown of the law of reflection if the disordered edge band overlaps with the Fermi level. We propose to search for a transport signature of the breakdown of the law of reflection in the magnetic focusing experiment sketched in Fig. 1. The idea is to study the reflection of ballistic cyclotron trajectories in a magnetic field B off a graphene edge [9, 14, 15]. The use of a collimator could improve such an experiment [16].

Magnetic focusing refers to the appearance of peaks in the nonlocal conductance between the source and the drain when a voltage is applied between the source and

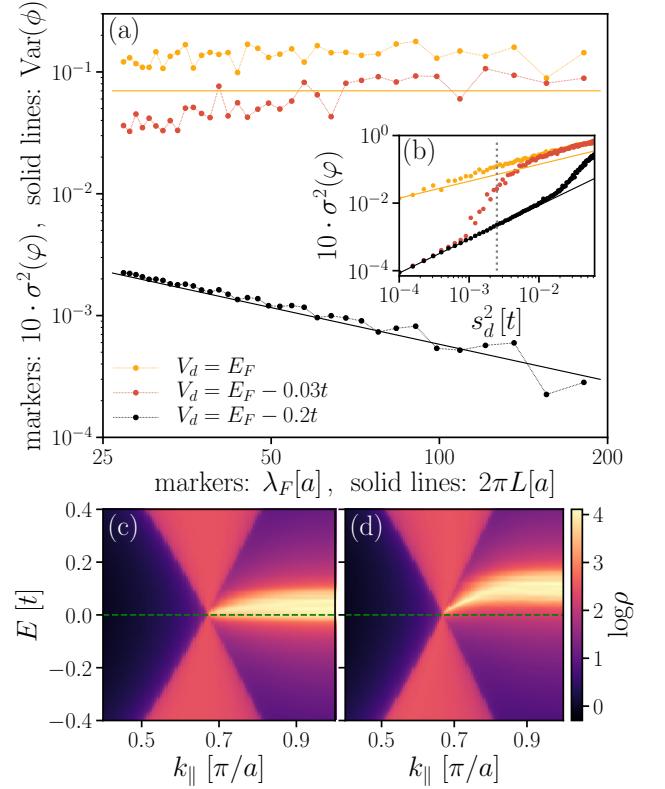


FIG. 2. (a) Solid lines: $\text{Var}(\phi)$ at the Dirac points ($E_F = 0$) as a function of the boundary length L , for a disorder strength $s_d = 0.05t$ obtained from the tight-binding model. Markers: $\sigma^2(\varphi)$ at finite E_F , averaged over all incoming modes and 10^2 disorder configurations, as a function of the Fermi wavelength λ_F for the same disorder strength, obtained numerically for a semi-infinite graphene sheet with a boundary of length $L = 300a$. The values chosen for $\lambda_F = \sqrt{3}\pi a/E_F$ correspond to E_F ranging from $0.2t$ to $0.03t$. (b) Same as (a), as a function of the disorder strength s_d^2 , for a value of $2\pi L \approx 27a$ [$\lambda_F \approx 27a$, $E_F = 0.2t$]. The dotted line indicates the value of s_d used in (a). For $V_d = E_F$ the variances of both the scattering phase at $E_F = 0$ and the reflection angle at $E_F > 0$ increase linearly with s_d , independent of the Fermi wavelength, exhibiting the breakdown of the law of reflection. For $|V_d - E_F| \gtrsim s_d$, $\text{Var}(\phi)$ [$\sigma^2(\varphi)$] decays with increasing L [λ_F] as $1/L$ [$1/\lambda_F$] and increases quadratically with the disorder strength [as given by Eq. (6)]. Reflection is thus specular, but becomes diffusive for $|V_d - E_F| \lesssim s_d$. Setting V_d closer to E_F moves transition between the regimes of specular and diffusive reflection to smaller s_d . This is because of the overlap of E_F with the disorder-broadened edge band. (c), (d) Momentum-resolved density of states at the disordered zigzag edge of a semi-infinite graphene sheet with a boundary of length $L = 300a$. A band of edge states with bandwidth $\propto s_d = 0.05t$ extends between the Dirac cones, residing mostly at energy V_d , with $V_d = 0.03t$ in (c) and $V_d = 0.2t$ in (d) [dashed lines].

the grounded ribbon, cf. Fig. 1. There is an increased probability for electrons to end up in the drain whenever the separation W_x between source and drain matches an integer multiple of the cyclotron diameter $2r_c$, where

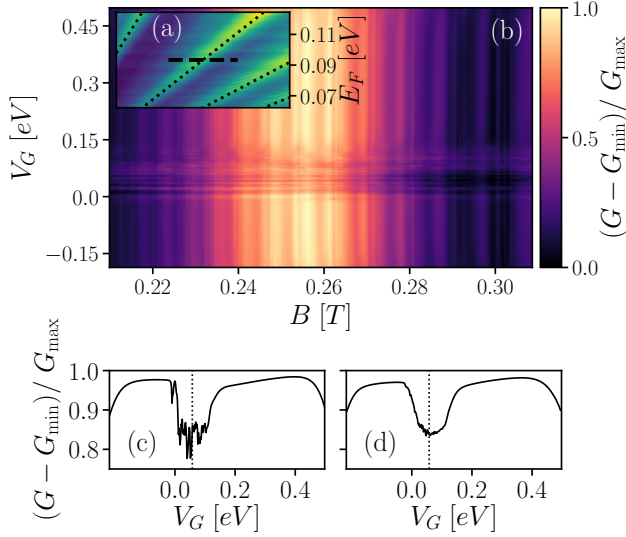


FIG. 3. (a) Conductance as a function of Fermi energy and magnetic field showing the first 4 magnetic focusing peaks for the device sketched in Fig. 1 in the absence of edge disorder and with $V_G = 0$. Superimposed are the predicted locations of the focusing peaks (dotted lines), $1 \leq p \leq 4$ from left to right across the diagonal. The color scale is linear and ranges from about $4e^2/h$ (dark) to $28e^2/h$ (bright). (b) Conductance around the $p = 2$ focusing peak at $E_F = 0.093$ eV [dashed line in (a)] versus gate voltage. We include disorder with $V_d = 0.062$ eV and $s_d = 0.047$ eV in the first $N = 6$ rows next to the boundary. Reflection at the boundary is specular and the conductance smooth in V_G , except for a dip when the disordered edge band overlaps with the Fermi level, and reflection becomes diffusive. (c) Line cut from (b) at $B = 0.256$ T with the predicted voltage value for the dip marked. Within the dip, the conductance exhibits fluctuations dependent on the particular disorder configuration, that are washed out by disorder averaging in (d). We assume the scaling factor $s = 9$ in the tight-binding model, such that $W_x = 1.6$ μm , $W_y = 1$ μm and $W_L = 0.2$ μm .

$r_c = \hbar k_F / eB$ is the cyclotron radius with k_F the Fermi momentum, \hbar the reduced Planck constant, and e the elementary charge. Due to the linear dispersion near the charge neutrality point in graphene, $k_F = E_F / \hbar v_F$ is linear in E_F , such that focusing peaks appear at the magnetic fields $B_n^f = 2nE_F / ev_F W_x$, $n \in \mathbb{N}$. For the setup in Fig. 1 but with a clean, specularly reflecting system edge, Fig. 3(a) shows a map of the first few focusing conductance peaks with their predicted locations marked. At resonance p , the electron beam reflects specularly $p - 1$ times at the system edge before exiting into the drain, as Fig. 1 demonstrates for $p = 2$. On the other hand, if reflection from the boundary is diffusive, the electrons scatter into random angles off the boundary, which in general no longer result in cyclotron trajectories that are commensurate with the distance from the focus point at the boundary to the drain. In comparison with the case of specular reflection, the focusing beam at the drain is

therefore diminished for diffusive edge scattering, resulting in a drop in the $p > 1$ conductance resonances. Because the reflection is diffusive when the disordered edge band overlaps with the Fermi level, by using a side gate (see Fig. 1) to tune the average potential at the disordered boundary, it is therefore possible to observe signatures of the breakdown of the law of reflection in the form of a conductance drop at a focusing peak.

To verify our prediction, we perform numerical simulations of the graphene focusing device with a side gate sketched in Fig. 1. We implement the tight-binding model for graphene in Kwant [28] and include the magnetic field via a Peierls substitution. We apply a random uniformly distributed onsite potential with mean V_d and variance s_d^2 to the first several rows of atoms adjacent to the system edge. We simulate the effect of a side gate by applying an extra potential with amplitude V_G exponentially decaying away from the sample edge on a length scale comparable to the size of the disordered region. Away from the charge neutrality point, we expect peak diffusive edge scattering to occur when the average potential by the boundary matches the Fermi energy. The relevant scales for our simulations are the hopping t , the graphene lattice constant $a = 2.46$ Å, and the magnetic flux $\Phi \propto Ba^2$ per unit cell. Scaling the tight-binding Hamiltonian with a scaling factor s [29] by reinterpreting $t/s \equiv t$, $sa \equiv a$ and $B/s^2 \equiv B$ such that Φ is unchanged by the scaling, our simulations apply to graphene devices of realistic and experimentally realizable dimensions [14, 15]. Note that the onsite disorder correlation length is not scale invariant, and the disorder thus correlates s lattice sites in the original model.

Tuning the average potential at the disordered system edge by varying the side gate V_G reveals a clear dip in the conductance Fig. 3(b) around the second focusing resonance $p = 2$, which is absent when no edge disorder is included [27]. Outside the dip the conductance only changes weakly with V_G , which is the expected behavior for a clean specularly reflecting boundary. Here, the first $N = 6$ rows of sites adjacent to the edge are disordered, and the extent of the disordered region into the graphene sheet thus approximately $2.1a \ll \lambda_F \approx 18a$, such that the length scales are consistent with specular reflection. The conductance fluctuates erratically within the dip, as the line cut Fig. 3(c) taken from Fig. 3(b) at $B = 0.256$ T shows. These are universal conductance oscillations particular to an individual disorder configuration. They are washed out by disorder averaging as Fig. 3(d) shows, revealing an omnipresent conductance dip. Furthermore, the conductance dip appears when the disordered edge band overlaps with E_F , which is the condition for the breakdown of the law of reflection, with the V_G that aligns the band with E_F marked in Figs. 3(c) and 3(d).

Conclusion and discussion.—Our analysis of scattering at a disordered graphene boundary reveals a regime where specular reflection is suppressed in favor of diffusive

scattering. This counterintuitive conclusion holds even when conventional wisdom dictates that specular reflection should dominate and the boundary should act as a mirror, namely when a boundary is rough on a length scale smaller than the Fermi wavelength. The origin of this breakdown of the law of reflection is resonant scattering of the electron waves from a linear superposition of localized boundary states. Our calculations show that this phenomenon is detectable in transverse magnetic focusing experiments, by employing a side gate to tune the average potential at the boundary. In these experiments the breakdown of specular reflection manifests as a dip in the nonlocal conductance at the second focusing resonance. Because the zigzag boundary condition is generic in graphene, we expect our results to apply to an arbitrary termination direction, and to be insensitive to microscopic details. We are thus confident that this effect is experimentally observable in present-day devices.

This work was supported by ERC Starting Grant No. 638760, the Netherlands Organisation for Scientific Research (NWO/OCW), and the U.S. Office of Naval Research.

* Electronic address: elias.walter@rwth-aachen.de

† Electronic address: torosdahl@gmail.com

- [1] H. Davies, *Proc. Inst. Elec. Eng. IV* **101**, 209 (1954).
- [2] H. E. Bennett and J. O. Porteus, *J. Opt. Soc. Am.* **51**, 123 (1961).
- [3] A. K. Geim and K. S. Novoselov, *Nat. Mater.* **6**, 183 (2007).
- [4] A. H. Castro Neto, F. Guinea, N. M. R. Peres, K. S. Novoselov, and A. K. Geim, *Rev. Mod. Phys.* **81**, 109 (2009).
- [5] C. H. Lui, L. Liu, K. F. Mak, G. W. Flynn, and T. F. Heinz, *Nature* **462**, 339 (2009).
- [6] C. R. Dean, A. F. Young, I. Meric, C. Lee, L. Wang, S. Sorgenfrei, K. Watanabe, T. Taniguchi, P. Kim, K. L. Shepard, and J. Hone, *Nat. Nanotechnology* **5**, 722 (2010).
- [7] A. S. Mayorov, R. V. Gorbachev, S. V. Morozov, L. Britnell, R. Jalil, L. A. Ponomarenko, P. Blake, K. S. Novoselov, K. Watanabe, T. Taniguchi, and A. K. Geim, *Nano Lett.* **11**, 2396 (2011).
- [8] L. Banszerus, M. Schmitz, S. Engels, M. Goldsche, K. Watanabe, T. Taniguchi, B. Beschoten, and C. Stampfer, *Nano Lett.* **16**, 1387 (2016).
- [9] H. van Houten and C. Beenakker, in *Analogies in Optics and Micro Electronics*, edited by W. van Haeringen and D. Lenstra (Kluwer, Dordrecht, 1990) Chap. Quantum Point Contacts and Coherent Electron Focusing.
- [10] V. V. Cheianov, V. Fal'ko, and B. L. Altshuler, *Science* **315**, 1252 (2007).
- [11] S. Chen, Z. Han, M. M. Elahi, K. M. M. Habib, L. Wang, B. Wen, Y. Gao, T. Taniguchi, K. Watanabe, J. Hone, A. W. Ghosh, and C. R. Dean, *Science* **353**, 1522 (2016).
- [12] P. Rickhaus, P. Makk, M.-H. Liu, E. Tóvári, M. Weiss, R. Maurand, K. Richter, and C. Schönenberger, *Nat. Commun.* **6**, 6470 (2015).
- [13] T. Taychatanapat, J. Y. Tan, Y. Yeo, K. Watanabe, T. Taniguchi, and B. Özyilmaz, *Nat. Commun.* **6**, 6093 (2015).
- [14] T. Taychatanapat, K. Watanabe, T. Taniguchi, and P. Jarillo-Herrero, *Nature Phys.* **9**, 225 (2013).
- [15] S. Bhandari, G.-H. Lee, A. Kiales, K. Watanabe, T. Taniguchi, E. Heller, P. Kim, and R. M. Westervelt, *Nano Lett.* **16**, 1690 (2016).
- [16] A. W. Barnard, A. Hughes, A. L. Sharpe, K. Watanabe, T. Taniguchi, and D. Goldhaber-Gordon, *Nat. Commun.* **8**, 15418 EP (2017).
- [17] Y.-W. Son, M. L. Cohen, and S. G. Louie, *Phys. Rev. Lett.* **97**, 216803 (2006).
- [18] D. Halbertal, M. Ben Shalom, A. Uri, K. Bagani, A. Y. Meltzer, I. Marcus, Y. Myasoedov, J. Birkbeck, L. S. Levitov, A. K. Geim, and E. Zeldov, *Science* **358**, 1303 (2017).
- [19] D. A. Areshkin, D. Gunlycke, and C. T. White, *Nano Lett.* **7**, 204 (2007).
- [20] M. Evaldsson, I. V. Zozoulenko, H. Xu, and T. Heinzel, *Phys. Rev. B* **78**, 161407 (2008).
- [21] S. Masubuchi, K. Iguchi, T. Yamaguchi, M. Onuki, M. Arai, K. Watanabe, T. Taniguchi, and T. Machida, *Phys. Rev. Lett.* **109**, 036601 (2012).
- [22] V. K. Dugaev and M. I. Katsnelson, *Phys. Rev. B* **88**, 235432 (2013).
- [23] A. R. Akhmerov and C. W. J. Beenakker, *Phys. Rev. B* **77**, 085423 (2008).
- [24] M. V. Berry and R. J. Mondragon, *Proc. R. Soc. A* **412**, 53 (1987).
- [25] E. McCann and V. I. Fal'ko, *J. Phys. Condens. Matter* **16**, 2371 (2004).
- [26] J. A. M. van Ostaay, A. R. Akhmerov, C. W. J. Beenakker, and M. Wimmer, *Phys. Rev. B* **84**, 195434 (2011).
- [27] See supplementary material.
- [28] C. W. Groth, M. Wimmer, A. R. Akhmerov, and X. Waintal, *New J. Phys.* **16**, 063065 (2014).
- [29] M.-H. Liu, P. Rickhaus, P. Makk, E. Tóvári, R. Maurand, F. Tkatschenko, M. Weiss, C. Schönenberger, and K. Richter, *Phys. Rev. Lett.* **114**, 036601 (2015).

I. SUPPLEMENT

A. Computation of the scattering phase in the continuum description

In the following, we present the derivation of the scattering phase at $E_F = 0$ from the continuum description governed by the Dirac equation, which is valid within the linear regime of the graphene dispersion.

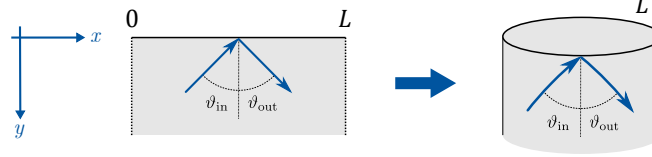


FIG. S1. Scheme of the system geometry: A graphene sheet (gray) with translational invariance in y -direction is terminated by a single boundary at $y = 0$. Applying periodic boundary conditions (left, dotted lines) in x -direction on the semi-infinite plane is equivalent to rolling it up to a cylinder (right). L is the boundary length after applying periodic boundary conditions. Blue arrows indicate schematically the paths of an incoming and an outgoing mode, with angles relative to the surface normal of ϑ_{in} and ϑ_{out} , respectively.

We consider a cylindrical geometry as sketched in Fig. S1 with a boundary of length L , which in the limit $L \rightarrow \infty$ resembles a semi-infinite sheet with a single boundary at $y = 0$. We describe electronic properties in terms of the Dirac Hamiltonian of a single valley,

$$H = v_F \boldsymbol{\sigma} \cdot \mathbf{p} = -i\hbar v_F \begin{pmatrix} 0 & \partial_x - i\partial_y \\ \partial_x + i\partial_y & 0 \end{pmatrix}, \quad (\text{S1})$$

as defined in the main text. With the ansatz $\psi(\mathbf{r}) = e^{i\mathbf{q}\cdot\mathbf{r}} (\psi_A, \psi_B)^T$ we obtain from the Dirac equation at zero energy $H\psi = 0$

$$\begin{cases} (q_x - iq_y)\psi_B = 0, \\ (q_x + iq_y)\psi_A = 0. \end{cases} \quad (\text{S2})$$

Periodic boundary conditions in x -direction $\psi(x, y) = \psi(x + L, y)$ restrict the momentum $q_x = 2\pi n/L$, with $n \in \mathbb{Z}$. With the boundary at $y = 0$ and the graphene sheet extending to positive y as shown in Fig. S1, we can write down all non-trivial solutions of Eq. (S2) for given n . We can distinguish two cases, depending on the behavior for $y \rightarrow \infty$:

For $n = 0$ we have $\mathbf{q} = 0$ and therefore all states $\psi = (\psi_A, \psi_B)^T$ are solutions to the Dirac equation (S2). We can choose an orthonormal basis $\{\psi_+, \psi_-\}$ of that two-dimensional subspace that diagonalizes the y -component of the current operator $\mathbf{J} = v_F \boldsymbol{\sigma}$, such that ψ_{\pm} have well-defined current $\pm v_F$ perpendicular to the boundary,

$$\psi_{\eta}^{\dagger} \mathbf{J}_y \psi_{\nu} = \eta v \delta_{\eta\nu}, \quad \eta, \nu = \pm, \quad (\text{S3})$$

$$\psi_{\eta}^{\dagger} \psi_{\nu} = \delta_{\eta\nu}. \quad (\text{S4})$$

The propagating modes are therefore the eigenstates of σ_y that can be written as $\psi_{\pm} = \frac{1}{\sqrt{2}}(1, \pm i)^T$. As ψ_- has a velocity $-v_F$ and is thus moving in negative y -direction, we consider it to be incoming and ψ_+ to be outgoing, respectively.

For $n \neq 0$ the Dirac equation (S2) becomes

$$\begin{cases} (2\pi n/L - iq_y)\psi_B = 0, \\ (2\pi n/L + iq_y)\psi_A = 0. \end{cases} \quad (\text{S5})$$

such that we get two non-trivial solutions for each n : For $q_y = -2\pi i n/L$ and $\psi_A = 0$ we have $\psi_{n,-} = e^{2\pi i n x/L} e^{2\pi n y/L} (0, 1)^T$. This mode decays exponentially into the bulk for $y \rightarrow \infty$ if $n < 0$, but is not normalizable for positive y if $n > 0$. For $q_y = 2\pi i n/L$ and $\psi_B = 0$ we have $\psi_{n,+} = e^{2\pi i n x/L} e^{-2\pi n y/L} (1, 0)^T$. This mode is evanescent if $n > 0$, but not normalizable if $n < 0$. In total we thus remain with one evanescent mode for each $n \in \mathbb{Z} \setminus \{0\}$.

We can now construct a scattering state ψ from the incoming mode ψ_- , outgoing mode ψ_+ and evanescent modes $\psi_{n,\pm}$ as

$$\psi = \psi_- + S\psi_+ + \sum_{n=1}^{\infty} (\alpha_n \psi_{n,+} + \alpha_{-n} \psi_{-n,-}), \quad (\text{S6})$$

where $S = e^{i\phi}$ is the scattering phase that the incoming mode acquires when scattered into the outgoing one, and α_n is the amplitude to scatter into the n -th evanescent mode. A boundary is introduced by requiring this scattering state to fulfill the boundary condition

$$M\psi(x, y=0) = \psi(x, y=0). \quad (\text{S7})$$

A disordered boundary interpolating between a clean zigzag boundary and an infinite-mass (Berry-Mondragon [24]) boundary condition constitutes the most general single-valley boundary condition. This boundary condition applies to different microscopic origins of disorder, such as the staggered potential on a zigzag boundary which is produced by a passivation of the dangling bonds [23], or effects of edge reconstruction [26]. The zigzag boundary is given by the matrix $M_{zz} = \sigma_z$, whereas the Berry-Mondragon boundary is specified by $M_{\text{BM}} = \boldsymbol{\sigma} \cdot (\hat{\mathbf{z}} \times \mathbf{n}_B) = \sigma_x$ for the boundary normal $\mathbf{n}_B = -\hat{\mathbf{y}}$. We therefore consider the boundary condition matrix

$$M = \cos \theta(x) M_{zz} + \sin \theta(x) M_{\text{BM}} = \begin{pmatrix} \cos \theta(x) & \sin \theta(x) \\ \sin \theta(x) & -\cos \theta(x) \end{pmatrix}, \quad (\text{S8})$$

with a random function $\theta(x)$ to introduce disorder by a spatially fluctuating staggered potential, such that we obtain a zigzag boundary for $\theta = 0$ and an infinite-mass boundary for $\theta = \pi/2$. The value of $\theta(x)$ at the position x on the boundary is randomly taken from a Gaussian distribution with mean value θ_0 and variance s_θ^2 . Furthermore, we assume a Gaussian correlation in space,

$$\text{Cov}[\theta(x), \theta(x')] = s_\theta^2 e^{-\pi(x-x')^2/d^2}, \quad (\text{S9})$$

with a correlation length d that corresponds to a lattice constant, since the real problem lives on a lattice. In the limit $d \rightarrow 0$ the correlations become $\text{Cov}[\theta(x), \theta(x')] \rightarrow s_\theta^2 d \delta(x-x')$.

With $\psi(x, y=0) = (\psi_A(x), \psi_B(x))^T$ we obtain from the boundary condition Eq. (S7)

$$\mu(x) \sum_{n=0}^{\infty} \alpha_n e^{2\pi i n x/L} - \sum_{n=-1}^{-\infty} \alpha_n e^{2\pi i n x/L} - i\alpha_0 = -i\sqrt{2}, \quad (\text{S10})$$

with $\mu(x) = \tan(\theta(x)/2)$ (being 0 for a clean zigzag and 1 for the infinite-mass type boundary) and $\alpha_0 = (1+S)/\sqrt{2}$. We Fourier-transform Eq. (S10) by applying to both sides $\frac{1}{L} \int_0^L dx e^{-2\pi i m x/L}$, with $m \in \mathbb{Z}$, to obtain

$$\sum_{n=1}^{\infty} \tilde{\mu}_{n-m} \alpha_n + (\tilde{\mu}_{-m} - i\delta_{m,0}) \alpha_0 - \sum_{n=-1}^{-\infty} \delta_{m,n} \alpha_n = -i\sqrt{2} \delta_{m,0}, \quad (\text{S11})$$

with the Fourier components of the disorder function μ ,

$$\tilde{\mu}_m = \frac{1}{L} \int_0^L dx e^{2\pi i m x/L} \mu(x), \quad m \in \mathbb{Z}. \quad (\text{S12})$$

We can rephrase Eq. (S11) in matrix form as

$$\underbrace{\begin{pmatrix} \tilde{\boldsymbol{\mu}} & \tilde{\mu}_\uparrow & 0 \\ \tilde{\mu}_\uparrow^\dagger & \tilde{\mu}_0 - i & 0 \\ \tilde{\boldsymbol{\mu}}' & \tilde{\mu}_\downarrow & -\mathbb{1} \end{pmatrix}}_{\tilde{\mathbf{A}}} \cdot \begin{pmatrix} \alpha_+ \\ \alpha_0 \\ \alpha_- \end{pmatrix} = \begin{pmatrix} 0 \\ -i\sqrt{2} \\ 0 \end{pmatrix}, \quad (\text{S13})$$

with

$$\alpha_+ = \begin{pmatrix} \vdots \\ \alpha_3 \\ \alpha_2 \\ \alpha_1 \end{pmatrix}, \quad \alpha_- = \begin{pmatrix} \alpha_{-1} \\ \alpha_{-2} \\ \alpha_{-3} \\ \vdots \end{pmatrix}, \quad \text{and} \\ \tilde{\boldsymbol{\mu}} = \begin{pmatrix} \ddots & \ddots & \ddots & \vdots \\ \ddots & \tilde{\mu}_0 & \tilde{\mu}_1^* & \tilde{\mu}_2^* \\ \ddots & \tilde{\mu}_1 & \tilde{\mu}_0 & \tilde{\mu}_1^* \\ \cdots & \tilde{\mu}_2 & \tilde{\mu}_1 & \tilde{\mu}_0 \end{pmatrix}, \quad \tilde{\boldsymbol{\mu}}' = \begin{pmatrix} \cdots & \tilde{\mu}_4 & \tilde{\mu}_3 & \tilde{\mu}_2 \\ \ddots & \tilde{\mu}_5 & \tilde{\mu}_4 & \tilde{\mu}_3 \\ \ddots & \tilde{\mu}_6 & \tilde{\mu}_5 & \tilde{\mu}_4 \\ \ddots & \ddots & \ddots & \vdots \end{pmatrix}, \quad \tilde{\mu}_\uparrow = \begin{pmatrix} \vdots \\ \tilde{\mu}_3^* \\ \tilde{\mu}_2^* \\ \tilde{\mu}_1^* \end{pmatrix}, \quad \tilde{\mu}_\downarrow = \begin{pmatrix} \tilde{\mu}_1 \\ \tilde{\mu}_2 \\ \tilde{\mu}_3 \\ \vdots \end{pmatrix}. \quad (\text{S14})$$

Hence, we have transformed the general boundary condition Eq. (S7) into a system of equations for the scattering phase (expressed through α_0). This system is specified by the Fourier coefficients of the disorder function μ . To solve Eq. (S13) for S , we have to invert $\tilde{\mathbf{A}}$ to obtain $S = \sqrt{2}\alpha_0 - 1 = -1 - 2i(\tilde{\mathbf{A}}^{-1})_{0,0}$, where $(\tilde{\mathbf{A}}^{-1})_{0,0}$ is the component in the center of $\tilde{\mathbf{A}}^{-1}$, referring to the $n = m = 0$ Fourier components.

Due to the Gaussian correlation of $\theta(x)$ in space (Eq. (S9)), the Fourier components $\tilde{\theta}_n = \frac{1}{L} \int_0^L dx e^{2\pi i n x/L} \theta(x)$ decay for large n ,

$$\mathbb{E}[\tilde{\theta}_n] = \theta_0 \delta_{n,0}, \quad \text{Cov}[\tilde{\theta}_n^*, \tilde{\theta}_m] \stackrel{d \ll L}{\approx} \delta_{n,m} \frac{s_\theta^2}{\sqrt{2\pi n_0^2}} e^{-n^2/2n_0^2}, \quad (\text{S15})$$

on a length scale $n_0 = L/\sqrt{2\pi}d$. The same holds for $\tilde{\mu}_n$, hence we can imagine to cut off at some $N \gg n_0$, such that the matrices in Eq. (S14) are finite-dimensional and we can safely use standard formulae for block-wise matrix inversion to formally obtain

$$S = \frac{i - \tilde{m}}{i + \tilde{m}}, \quad (\text{S16})$$

with $\tilde{m} = \tilde{\mu}_\uparrow^\dagger \tilde{\mu}^{-1} \tilde{\mu}_\uparrow - \tilde{\mu}_0$, and therefore

$$\phi = \arg(S) = \text{atan2}(\Re(S), \Im(S)) = \text{atan2}(1 - \tilde{m}^2, 2\tilde{m}), \quad (\text{S17})$$

where the atan2-function is closely related to the arctangent but adjusted such that it properly gives the angle between its arguments.

The inversion of $\tilde{\mu}$ is not generically possible. However, an approximate solution can be found when $\tilde{\mu}$ is dominated by its diagonal. We split up $\theta(x)$ into its mean value and fluctuations, $\theta(x) = \theta_0 + \delta\theta(x)$, with

$$\mathbb{E}[\delta\theta(x)] = 0, \quad (\text{S18})$$

$$\text{Cov}[\delta\theta(x), \delta\theta(x')] = s_\theta^2 e^{-\pi(x-x')^2/d^2}, \quad (\text{S19})$$

according to Eq. (S9). Assuming the disorder to be weak, $s_\theta \ll 1$, we can similarly expand $\mu(x) = \tan(\theta(x)/2)$ to get

$$\begin{aligned} \mu(x) &= \tan\left(\frac{\theta_0}{2}\right) + \frac{1 + \tan^2\left(\frac{\theta_0}{2}\right)}{2} \delta\theta(x) + \mathcal{O}(\delta\theta(x)^2) \\ &= \mu_0 + \delta\mu(x) + \mathcal{O}(\delta\mu(x)^2). \end{aligned} \quad (\text{S20})$$

The Fourier coefficients read

$$\tilde{\mu}_n = \mu_0 \delta_{n,0} + s_\mu \tilde{x}_n, \quad (\text{S21})$$

where

$$s_\mu = \frac{1 + \tan^2\left(\frac{\theta_0}{2}\right)}{2} s_\theta \quad (\text{S22})$$

is the standard deviation of μ and

$$\tilde{x}_n = \frac{1}{L} \int_0^L dx e^{2\pi i n x/L} \frac{\delta\mu(x)}{s_\mu} \quad (\text{S23})$$

is normalized to have variance 1 and by definition a mean value of 0. Furthermore, from Eq. (S15) we see that

$$\text{Cov}(\tilde{x}_n^*, \tilde{x}_m) \stackrel{d \ll L}{\approx} \delta_{n,m} \frac{1}{\sqrt{2\pi n_0^2}} e^{-n^2/2n_0^2}. \quad (\text{S24})$$

With Eq. (S21) we get

$$\tilde{\mu} = \mu_0 \mathbb{1}_N + s_\mu \tilde{\mathbf{x}}, \quad (\text{S25})$$

thereby splitting it up into a diagonal part which is trivial to invert and a random Toeplitz matrix

$$\tilde{\mathbf{x}} = \begin{pmatrix} \ddots & \ddots & \vdots \\ \ddots & \tilde{x}_0 & \tilde{x}_1^* \\ \ddots & \tilde{x}_1 & \tilde{x}_0 \end{pmatrix}, \quad (\text{S26})$$

that cannot be inverted explicitly analytically.

For $\theta_0 = 0 = \mu_0$, the disorder potential $\theta(x)$ is zero on average such that the disorder-broadened edge states overlap with $E = 0$, whereas a finite $\theta_0 > s_\theta$ (or $\mu_0 > s_\mu$) shifts them away from $E = 0$. We can directly translate these two cases to the structure of $\tilde{\boldsymbol{\mu}}$:

- For finite μ_0 with small fluctuations s_μ on top, $\tilde{\boldsymbol{\mu}}$ is dominated by its diagonal. Hence, we can expand its inverse in powers of s_μ . In this case, where the law of reflection is expected to hold, we can therefore give an explicit expression for ϕ for sufficiently weak disorder.
- For a boundary with $\mu_0 = 0$ that fulfills the condition for diffusive scattering, this consideration does not work as then $\tilde{\boldsymbol{\mu}} = s_\mu \tilde{\mathbf{x}}$. In this case we have to rely on a numerical analysis.

1. Scattering phase if law of reflection holds

In the limit where $s_\mu \ll \mu_0$, we can expand

$$\tilde{\boldsymbol{\mu}}^{-1} = \frac{1}{\mu_0} \mathbb{1} - \frac{s_\mu}{\mu_0^2} \tilde{\mathbf{x}} + \mathcal{O}\left(\frac{s_\mu^2}{\mu_0^2}\right) \quad (\text{S27})$$

to obtain

$$\tilde{m} = -\mu_0 - s_\mu \tilde{x}_0 + \frac{s_\mu^2}{\mu_0} \sum_{n=1}^{\infty} |\tilde{x}_n|^2 + \mathcal{O}\left(\frac{s_\mu^3}{\mu_0^3}\right). \quad (\text{S28})$$

Expanding ϕ in powers of s_μ/μ_0 , we get with Eqs. (S20) and (S22)

$$\phi = -\theta_0 - s_\theta \tilde{x}_0 + \frac{1}{2} \left(\tilde{x}_0^2 + \frac{1}{\sin^2(\frac{\theta_0}{2})} \sum_{n=1}^{\infty} |\tilde{x}_n|^2 \right) \tan\left(\frac{\theta_0}{2}\right) s_\theta^2 + \mathcal{O}\left(\frac{s_\theta^3}{\theta_0^3}\right). \quad (\text{S29})$$

Knowing the distribution of \tilde{x}_n (Eq. (S24)), we can average over all \tilde{x}_n to compute mean value and variance of ϕ . We obtain

$$\text{E}[\phi] = -\theta_0 + \frac{s_\theta^2}{2 \sin(\theta_0)} - \frac{d}{L} \frac{s_\theta^2}{2 \tan(\theta_0)} + \mathcal{O}\left(\frac{s_\theta^3}{\theta_0^3}\right), \quad (\text{S30})$$

$$\text{Var}(\phi) = \frac{ds_\theta^2}{L} + \mathcal{O}\left(\frac{s_\theta^3}{\theta_0^3}\right). \quad (\text{S31})$$

2. Scattering phase for broken law of reflection

For $\mu_0 = 0$, where the disorder-broadened edge states overlap with the Fermi energy $E = 0$, we have $\tilde{\boldsymbol{\mu}} = s_\mu \tilde{\mathbf{x}}$, and hence with Eqs. (S21), (S22)

$$\tilde{m} = \frac{s_\theta}{2} \chi, \quad \text{with} \quad \chi = \tilde{x}_\uparrow^\dagger \tilde{\mathbf{x}}^{-1} \tilde{x}_\uparrow - \tilde{x}_0. \quad (\text{S32})$$

We obtain

$$\phi = \text{atan2}\left(1 - s_\theta^2 \chi^2 / 4, s_\theta \chi\right). \quad (\text{S33})$$

For small s_θ we have $\phi = s_\theta \chi + \mathcal{O}(s_\theta^3)$, hence the distribution of ϕ is directly linked to the distribution of χ , which we will now further explore.

Due to Eq. (S24), the elements of $\tilde{\mathbf{x}}$ decay away from the diagonal, $E[|\tilde{x}_n|^2] \sim \exp(-n^2/2n_0^2)$. In the limit $n_0 \rightarrow 0$, which corresponds to the limit $d/L \rightarrow \infty$, *i.e.*, completely correlated (constant) disorder, the matrix $\tilde{\mathbf{x}}$ will therefore be essentially diagonal. In 0th order we have $\tilde{\mathbf{x}} = \tilde{x}_0 \mathbb{1}$, and therefore

$$\chi = \frac{\sum_{n=1}^{\infty} |\tilde{x}_n|^2}{\tilde{x}_0} - \tilde{x}_0. \quad (\text{S34})$$

Assuming the \tilde{x}_n to still be approximately independent (although the approximation made in Eq. (S24) does not hold in the limit $d/L \rightarrow \infty$), due to the central limit theorem the numerator and denominator are independent Gaussian distributed variables, with zero (or approximately zero) mean. As a result, the first term χ_1 of Eq. (S34) follows a Cauchy distribution

$$f_{\chi_1}(x) = \frac{1}{\pi} \frac{\gamma}{x^2 + \gamma^2}. \quad (\text{S35})$$

However, its scale parameter scales as $\gamma \sim \exp(-1/n_0^2)$, therefore in the limit $n_0 \rightarrow 0$ we remain with the second term χ_0 of Eq. (S34), $\chi = \chi_0 = -\tilde{x}_0$. In the limit $d/L \rightarrow \infty$ the approximation of Eq. (S24) does not hold for \tilde{x}_0 ; instead we find $\text{Var}(\tilde{x}_0) = 1$, such that ϕ is normally distributed with mean 0 and variance s_θ^2 .

In fact, we are however interested in the distribution of ϕ in the opposite limit, $L/d \rightarrow \infty$. In this limit $\chi_0 = -\tilde{x}_0$ becomes small, $\text{Var}(\tilde{x}_0) = 1/\sqrt{2\pi n_0^2} = d/L$, whereas we find numerically that χ_1 still follows a Cauchy distribution, with a scale parameter γ that becomes independent of L/d and can be evaluated numerically as $\gamma \approx 0.8 s_\theta$. Remarkably, the value of γ/s_θ we obtain numerically is not universal, but depends weakly on the original distribution of the disorder $\theta(x)$. If we choose these parameters to be not normally distributed but to follow any other distribution, χ is still Cauchy distributed, but the scale parameter γ will also depend on the higher cumulants of the chosen disorder distribution.

Based on this distribution, we can evaluate mean value and variance of the scattering phase ϕ . Since f_{χ_1} is even and ϕ is an odd function of χ , we directly see that $E[\phi] = 0$. Furthermore, we can numerically evaluate the integral in $E[\phi^2]$ to obtain

$$\text{Var}(\phi) \approx 2.2 s_\theta. \quad (\text{S36})$$

B. Computation of the scattering matrix from the tight-binding model

1. Tight-binding Hamiltonian

To extend the consideration to the more general case of two Dirac valleys, we compute the scattering matrix from an atomistic tight-binding model with nearest neighbor hopping $t \approx 2.8 \text{ eV}$, with a geometry as shown in Fig. S2, in direct analogy to Fig. S1. Disorder is included by introducing Gaussian distributed random on-site potentials V_n on the boundary site n with mean V_d and variance s_d^2 . The corresponding Hamiltonian is

$$H = -t \sum_{\langle mnj, m'n'j' \rangle} |m, n, j\rangle \langle m', n', j'| + \sum_n V_n |0, n, 4\rangle \langle 0, n, 4| \quad (\text{S37})$$

where the brackets under the first sum indicate that it goes only over nearest neighbors. According to Fig. S2, each lattice site is specified by three indices: m labels the y -coordinate of the blue rectangular superlattice shown in Fig. S2 from 1 to ∞ within the lead, being 0 on the boundary sites, n labels the corresponding x -coordinate from 0 to $N-1 = (L-1)/a$, with the boundary length L and lattice constant a , and j determines the position within each cell of the superlattice in the order specified in Fig. S2. The atomic orbitals $\{|m, n, j\rangle\}$ are assumed to form a complete basis of the lead Hilbert space within the tight-binding approximation. Therefore, any state on the lead can be written as

$$|\psi_L\rangle = \sum_{m=1}^{\infty} \sum_{n=0}^{N-1} \sum_{j=1}^4 \psi_L(m, n, j) |m, n, j\rangle, \quad (\text{S38})$$

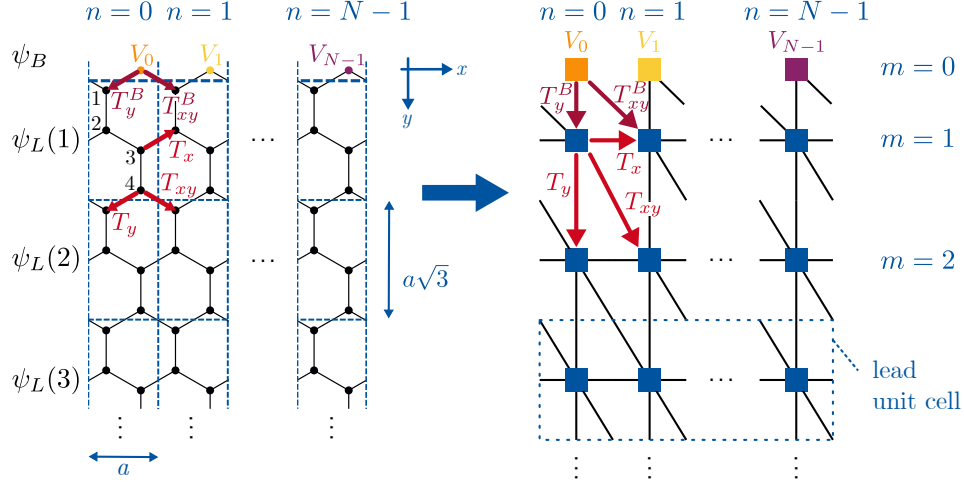


FIG. S2. Scheme of the tight-binding system for which the scattering matrix is computed, introducing a rectangular superlattice with four sites per unit cell. The superlattice unit cells are represented by blue squares in the right picture, defining a tight-binding system based on this superlattice. n labels the x -coordinate along the boundary from 0 to $N - 1 = (L - 1)/a$ and m is the corresponding y -index going from 1 to ∞ as the lead has translational invariance in y -direction. The index $m = 0$ indicates the boundary sites that do not belong to the lead. Numbers in the (1,1) unit cell (left) specify the order of the sites within each unit cell in the vector representation that will be used. As indicated by half lines, periodic boundary conditions are implemented by connecting the $n = N - 1$ to the $n = 0$ cells. V_n is the onsite disorder potential on the n -th boundary site and the T -s are the hopping matrices between adjacent superlattice unit cells within the lead and between lead and boundary (indicated by superscript B). ψ_B is the wavefunction amplitude on the boundary sites and $\psi_L(m)$ the one on the m -th unit cell of the lead (m -th row of the superlattice).

where $\psi_L(m, n, j) = \langle m, n, j | \psi_L \rangle$ is the amplitude of the lead wavefunction on the lattice site (m, n, j) . Correspondingly, the state on the boundary is given by the orbital states on the boundary sites as

$$|\psi_B\rangle = \sum_{n=0}^{N-1} \psi_B(n) |0, n, 4\rangle \quad (\text{S39})$$

with an amplitude $\psi_B(n) = \langle 0, n, 4 | \psi_B \rangle$ on the n -th boundary site. We can write the combined wavefunction $\psi = \psi_L + \psi_B$ in a vector representation within this basis as

$$\psi = \begin{pmatrix} \psi_L \\ \psi_B \end{pmatrix} = \begin{pmatrix} \vdots \\ \psi_L(2, N-1) \\ \vdots \\ \psi_L(2, 0) \\ \psi_L(1, N-1) \\ \vdots \\ \psi_L(1, 0) \\ \psi_B(N-1) \\ \vdots \\ \psi_B(0) \end{pmatrix}, \quad \psi_L(m, n) = \begin{pmatrix} \psi_L(m, n, 1) \\ \psi_L(m, n, 2) \\ \psi_L(m, n, 3) \\ \psi_L(m, n, 4) \end{pmatrix}. \quad (\text{S40})$$

The tight-binding Hamiltonian Eq. (S37) in matrix form reads

$$H = \begin{pmatrix} \ddots & \ddots & & & \\ \ddots & H_L & T_L & & \\ & T_L^\dagger & H_L & T_{LB} & \\ & & T_{LB}^\dagger & H_B & \end{pmatrix}. \quad (\text{S41})$$

Here

$$H_L = \begin{pmatrix} H_0 & T_x & & T_x^\dagger \\ T_x^\dagger & H_0 & \ddots & \\ & \ddots & \ddots & T_x \\ T_x & & T_x^\dagger & H_0 \end{pmatrix}, \quad H_B = \begin{pmatrix} V_{N-1} & & & \\ & \ddots & & \\ & & V_1 & \\ & & & V_0 \end{pmatrix} \quad (\text{S42})$$

are the $4N \times 4N$ Hamiltonian submatrix of each lead unit cell (row of the superlattice in Fig. S2, with fixed index $m \geq 1$) and the $N \times N$ submatrix of the boundary (containing the onsite disorder potential on the diagonal), respectively, and

$$T_L = \begin{pmatrix} T_y & T_{xy} & & \\ & T_y & \ddots & \\ & & \ddots & T_{xy} \\ T_{xy} & & & T_y \end{pmatrix}, \quad T_{LB} = \begin{pmatrix} T_y^B & T_{xy}^B & & \\ & T_y^B & \ddots & \\ & & \ddots & T_{xy}^B \\ T_{xy}^B & & & T_y^B \end{pmatrix} \quad (\text{S43})$$

couple consecutive lead unit cells and the $m = 1$ lead unit cell to the boundary, respectively. Their corresponding subblocks are given in terms of the hopping parameter t by

$$H_0 = \begin{pmatrix} 0 & -t & 0 & 0 \\ -t & 0 & -t & 0 \\ 0 & -t & 0 & -t \\ 0 & 0 & -t & 0 \end{pmatrix}, \quad T_x = \begin{pmatrix} 0 & 0 & 0 & 0 \\ 0 & 0 & -t & 0 \\ 0 & 0 & 0 & 0 \\ 0 & 0 & 0 & 0 \end{pmatrix}, \quad T_y = T_{xy} = \begin{pmatrix} 0 & 0 & 0 & -t \\ 0 & 0 & 0 & 0 \\ 0 & 0 & 0 & 0 \\ 0 & 0 & 0 & 0 \end{pmatrix}, \quad T_y^B = T_{xy}^B = \begin{pmatrix} -t \\ 0 \\ 0 \\ 0 \end{pmatrix}, \quad (\text{S44})$$

where H_0 contains all hoppings between sites within one superlattice unit cell and the T 's the hoppings between adjacent cells, as sketched in Fig. S2. For simplicity and to keep expressions shorter, we will from now on set $t = 1$, *i.e.*, all energies such as the disorder potential will be given in units of t .

2. Lead eigenstates

To solve for the scattering matrix, we first have to compute propagating and evanescent eigenstates of the tight-binding Hamiltonian on an infinite lead without a boundary, which is given by

$$H_L^{\text{inf}} = \begin{pmatrix} \ddots & \ddots & & \\ \ddots & H_L & T_L & \\ & T_L^\dagger & H_L & \ddots \\ & & \ddots & \ddots \end{pmatrix}, \quad \psi_L^{\text{inf}} = \begin{pmatrix} \vdots \\ \psi_L(2) \\ \psi_L(1) \\ \vdots \end{pmatrix}. \quad (\text{S45})$$

Since this infinite lead has translational invariance in x - and in y -direction, we use a Bloch ansatz for the lead wavefunction,

$$\psi_L^{\text{inf}}(m, n) = \lambda^m \xi^n \chi, \quad (\text{S46})$$

where λ and ξ are eigenvalues of the translation operator in y - and x -direction, respectively. The 4-vector χ gives the mode structure within each superlattice unit cell. Note that this Bloch ansatz lives on the rectangular superlattice. We thereby disregard the original honeycomb lattice structure and assume the hoppings T_x and T_y to be exactly aligned with the x - and y -axis, respectively, as shown in Fig. S2 on the right. This means that we choose the mode structure χ within a unit cell to be multiplied by a factor of ξ when hopping along T_x , by λ when hopping along T_y , and by $\xi\lambda$ for hoppings T_{xy} . This choice amounts to a specific gauge of the phase of the wavefunction. Hence, it is completely equivalent to choosing Bloch phases according to the honeycomb structure by, *e.g.*, assuming also a phase shift in y -direction for hoppings T_x .

As we have periodic boundary conditions $\psi_L^{\text{inf}}(m, n) = \psi_L^{\text{inf}}(m, n + N)$, it must hold that $\xi^N = 1$, therefore we have

$$\xi_\nu = e^{ik_{x,\nu}a} = e^{2\pi i \nu / N} \quad \text{with} \quad k_{x,\nu} = \frac{2\pi \nu}{L} = \frac{2\pi}{a} \frac{\nu}{N}, \quad \nu = 0, \dots, N-1. \quad (\text{S47})$$

At $E_F = 0$, the Fermi surface consists only of the Dirac points, so propagating modes have a momentum that lies at these points in momentum space. Therefore, the momentum $k_{x,\nu}$ must match the x -component of the Dirac points for some ν to have propagating modes at all, such that we demand $k_{x,\nu} = K_x = 2\pi/3a$ or $k_{x,\nu} = K'_x = -2\pi/3a$, since the Dirac points in this coordinate choice are given by $\mathbf{K} = 2\pi/3a(1, \sqrt{3})$, $\mathbf{K}' = 2\pi/3a(-1, \sqrt{3})$. We conclude that $N \stackrel{!}{=} 3\nu$, thus propagating modes are only possible if the boundary length L is a multiple of $3a$, which we in the following will assume to be true.

Using the Bloch ansatz, the Schrödinger equation for the infinite lead at $E_F = 0$ reduces to

$$H_L^{\text{inf}} \psi_L^{\text{inf}} = 0 \quad \xrightarrow{\text{Eq. (S46)}} \quad H_c \chi = 0, \quad (\text{S48})$$

with

$$H_c = H_0 + (\xi_\nu^{-1} T_x + \lambda^{-1} T_y + \xi_\nu^{-1} \lambda^{-1} T_{xy} + \text{h.c.}) . \quad (\text{S49})$$

By solving $\det H_c = 0$, we obtain the relations

$$\lambda_\nu^+ = \frac{(1 + \xi_\nu)^2}{\xi_\nu}, \quad \lambda_\nu^- = \frac{\xi_\nu}{(1 + \xi_\nu)^2} \quad (\text{S50})$$

between the translation operator eigenvalues ξ and λ that need to be fulfilled for H_c to have a zero eigenvalue. Thereby for each possible x -momentum $k_{x,\nu}$ we have two solutions for the momentum in y -direction defined through

$$\lambda_\nu = e^{ik_{y,\nu}a}. \quad (\text{S51})$$

As we in fact restrict the lattice to positive y , modes do not have to be normalizable for negative y . Therefore, we can allow for all λ with $|\lambda| \leq 1$, *i.e.*, for plane waves and modes that decay exponentially for $y \rightarrow \infty$.

We get the corresponding eigenmodes as

$$\chi_\nu^+ = \begin{pmatrix} 0 \\ -1 \\ 0 \\ 1 + \xi_\nu \end{pmatrix}, \quad \chi_\nu^- = \begin{pmatrix} -1 - \xi_\nu \\ 0 \\ \xi_\nu \\ 0 \end{pmatrix}. \quad (\text{S52})$$

Regarding their translation eigenvalue λ_ν^\pm , these lead eigenmodes can be classified as follows:

a. Propagating modes: Modes with $\xi_{\mathbf{K}} = \xi_{N/3} = e^{2\pi i/3}$ and $\xi_{\mathbf{K}'} = \xi_{2N/3} = e^{-2\pi i/3}$ have $\lambda = 1$ and thus are propagating (their amplitudes do not decay in y -direction). Defining

$$\Phi_{\text{pr}} = (\chi_{\mathbf{K}}^-, \chi_{\mathbf{K}}^+, \chi_{\mathbf{K}'}^-, \chi_{\mathbf{K}'}^+), \quad \Xi_{\text{pr}} = \text{diag}(\xi_{\mathbf{K}}, \xi_{\mathbf{K}}, \xi_{\mathbf{K}'}, \xi_{\mathbf{K}'}), \quad \Lambda_{\text{pr}} = \mathbb{1}_4, \quad (\text{S53})$$

the set of propagating modes on the m -th lead unit cell is given by

$$\Psi_{\text{pr}} \Lambda_{\text{pr}}^m = \begin{pmatrix} \Phi_{\text{pr}} \Xi_{\text{pr}}^{N-1} \\ \vdots \\ \Phi_{\text{pr}} \Xi_{\text{pr}} \\ \Phi_{\text{pr}} \end{pmatrix} \Lambda_{\text{pr}}^m. \quad (\text{S54})$$

To separate incoming and outgoing states, we have to find eigenstates of the particle current operator

$$J = \frac{2a}{\hbar} \Im(\Lambda_{\text{pr}}^* T_L) \quad (\text{S55})$$

within the set of propagating modes. Therefore we have to diagonalize

$$J_{\text{pr}} = \Psi_{\text{pr}}^\dagger J \Psi_{\text{pr}} = \frac{2a}{\hbar} \Psi_{\text{pr}}^\dagger \Im(\Lambda_{\text{pr}}^* T_L) \Psi_{\text{pr}} = \frac{a}{i\hbar} \Psi_{\text{pr}}^\dagger (T_L - T_L^\dagger) \Psi_{\text{pr}}. \quad (\text{S56})$$

J_{pr} can be straightforwardly evaluated from the definitions above, yielding

$$J = \frac{4}{\sqrt{3}} N v_F \begin{pmatrix} 0 & -\alpha & & \\ -\alpha^* & 0 & & \\ & & 0 & \alpha^* \\ & & \alpha & 0 \end{pmatrix}, \quad (\text{S57})$$

with the Fermi velocity $v_F = \sqrt{3}ta/2\hbar$ and $\alpha = \xi_{\mathbf{K}}^{1/4} = e^{i\pi/6}$. The eigenvalues of \mathbf{J} are $-\frac{4}{\sqrt{3}}Nv_F$ (corresponding to incoming modes) with normalized eigenvectors $\mathbf{v}_{\mathbf{K}}^- = \frac{1}{\sqrt{2}}(\alpha, 1, 0, 0)^T$ and $\mathbf{v}_{\mathbf{K}'}^- = \frac{1}{\sqrt{2}}(0, 0, -\alpha^*, 1)^T$, and $+\frac{4}{\sqrt{3}}Nv_F$ (corresponding to outgoing modes) with eigenvectors $\mathbf{v}_{\mathbf{K}}^+ = \frac{1}{\sqrt{2}}(-\alpha, 1, 0, 0)^T$ and $\mathbf{v}_{\mathbf{K}'}^+ = \frac{1}{\sqrt{2}}(0, 0, \alpha^*, 1)^T$. Since we sorted the propagating modes by the two valleys (Eq. (S53)) and these eigenvectors do not mix the subspaces of the two valleys, we can also assign each to a unique valley by labeling them \mathbf{K}, \mathbf{K}' .

To ensure that S is unitary, all propagating lead eigenmodes have to be properly normalized to carry the same probability current. However, as here all modes have already the same current eigenvalue according to its absolute value, we can choose any normalization that simplifies the calculation. With

$$\Phi_{\text{in}} = \Phi_{\text{pr}} \cdot (\mathbf{v}_{\mathbf{K}}^-, \mathbf{v}_{\mathbf{K}'}^-) / \sqrt{N}, \quad \Xi_{\text{in}} = \text{diag}(\xi_{\mathbf{K}}, \xi_{\mathbf{K}'}), \quad \Lambda_{\text{in}} = \mathbb{1}_2, \quad \text{and} \quad (\text{S58})$$

$$\Phi_{\text{out}} = \Phi_{\text{pr}} \cdot (\mathbf{v}_{\mathbf{K}'}^+, \mathbf{v}_{\mathbf{K}}^+) / \sqrt{N}, \quad \Xi_{\text{out}} = \text{diag}(\xi_{\mathbf{K}'}, \xi_{\mathbf{K}}), \quad \Lambda_{\text{out}} = \mathbb{1}_2, \quad (\text{S59})$$

we can therefore define incoming and outgoing modes with current normalized to $\mp 4v_F/\sqrt{3}$ and well-defined momenta $k_x = 2\pi/3, k_x = -2\pi/3$ on the m -th lead unit cell within the notation introduced in Eq. (S40) as

$$(\psi_{\mathbf{K}}^{\text{in}}(m), \psi_{\mathbf{K}'}^{\text{in}}(m)) = \Psi_{\text{in}} \Lambda_{\text{in}}^m = \begin{pmatrix} \Phi_{\text{in}} \Xi_{\text{in}}^{N-1} \\ \vdots \\ \Phi_{\text{in}} \Xi_{\text{in}} \\ \Phi_{\text{in}} \end{pmatrix} \Lambda_{\text{in}}^m, \quad (\text{S60})$$

$$(\psi_{\mathbf{K}'}^{\text{out}}(m), \psi_{\mathbf{K}}^{\text{out}}(m)) = \Psi_{\text{out}} \Lambda_{\text{out}}^m = \begin{pmatrix} \Phi_{\text{out}} \Xi_{\text{out}}^{N-1} \\ \vdots \\ \Phi_{\text{out}} \Xi_{\text{out}} \\ \Phi_{\text{out}} \end{pmatrix} \Lambda_{\text{out}}^m. \quad (\text{S61})$$

Note that we sort the outgoing modes in opposite order with respect to the valleys as the incoming modes. This is to ensure that they reflect time-reversal symmetry. Under time-reversal the velocity of the modes is reversed and the valleys are exchanged. Therefore, with this ordering the outgoing modes are the time-reversed incoming ones.

b. Evanescent modes: For $-N/3 < \nu < N/3$ holds $\lambda_{\nu}^- < 1$ and $\lambda_{\nu}^+ > 1$, thus χ_{ν}^- -modes are evanescent, whereas χ_{ν}^+ -modes are not normalizable. For $N/3 < \nu < 2N/3 = -N/3 \bmod N$ the opposite case is true. The normalization of the evanescent modes is irrelevant for the result of the calculation of S , therefore we multiply them with $1/\sqrt{N}$ which will later simplify prefactors. We can then simply write the set of evanescent modes within the m -th lead unit cell as

$$(\psi_{-\frac{N}{3}+1}^{\text{ev}}(m), \dots, \psi_{\frac{N}{3}-1}^{\text{ev}}(m), \psi_{\frac{N}{3}+1}^{\text{ev}}(m), \dots, \psi_{\frac{2N}{3}-1}^{\text{ev}}(m)) = \Psi_{\text{ev}} \Lambda_{\text{ev}} = (\Psi_{\text{ev}}^- \Lambda_{\text{ev}}^-, \Psi_{\text{ev}}^+ \Lambda_{\text{ev}}^+), \quad (\text{S62})$$

where

$$\Psi_{\text{ev}}^{\mp} = \frac{1}{\sqrt{N}} \begin{pmatrix} \Phi_{\text{ev}}^{\mp} (\Xi_{\text{ev}}^{\mp})^{N-1} \\ \vdots \\ \Phi_{\text{ev}}^{\mp} \Xi_{\text{ev}}^{\mp} \\ \Phi_{\text{ev}}^{\mp} \end{pmatrix}, \quad \Lambda_{\text{ev}} = \text{diag}(\Lambda_{\text{ev}}^-, \Lambda_{\text{ev}}^+), \quad (\text{S63})$$

with

$$\begin{aligned} \Phi_{\text{ev}}^- &= (\chi_{-\frac{N}{3}+1}^-, \dots, \chi_{\frac{N}{3}-1}^-), \quad \Xi_{\text{ev}}^- = \text{diag}(\xi_{-\frac{N}{3}+1}^-, \dots, \xi_{\frac{N}{3}-1}^-), \quad \Lambda_{\text{ev}}^- = \text{diag}(\lambda_{-\frac{N}{3}+1}^-, \dots, \lambda_{\frac{N}{3}-1}^-), \\ \Phi_{\text{ev}}^+ &= (\chi_{\frac{N}{3}+1}^+, \dots, \chi_{\frac{2N}{3}-1}^+), \quad \Xi_{\text{ev}}^+ = \text{diag}(\xi_{\frac{N}{3}+1}^+, \dots, \xi_{\frac{2N}{3}-1}^+), \quad \Lambda_{\text{ev}}^+ = \text{diag}(\lambda_{\frac{N}{3}+1}^+, \dots, \lambda_{\frac{2N}{3}-1}^+). \end{aligned} \quad (\text{S64})$$

3. Computation of the scattering matrix

Since we have two incoming and two outgoing modes at the Dirac points, the scattering matrix is 2×2 . It can be parametrized as

$$S = e^{i\phi} \begin{pmatrix} re^{i\Delta} & \sqrt{1-r^2} \\ \sqrt{1-r^2} & -re^{-i\Delta} \end{pmatrix}, \quad (\text{S65})$$

with three real parameters r , ϕ and Δ . The phase ϕ of the off-diagonal (intra-valley) elements is the direct analogue of the scattering phase within the single-valley continuum description.

To solve for the scattering matrix, we use the eigenstates of the infinite lead to compose scattering states in the lead, now assuming to have the boundary terminating the lead, which are given in the m -th lead unit cell by

$$\Psi_L(m) = (\psi_{\mathbf{K}}(m), \psi_{\mathbf{K}'}(m)) = \Psi_{\text{in}} \Lambda_{\text{in}}^m + \Psi_{\text{out}} \Lambda_{\text{out}}^m S + \Psi_{\text{ev}} \Lambda_{\text{ev}}^m S_{\text{ev}}, \quad (\text{S66})$$

Each of these two scattering states is a superposition of a fixed incoming mode with momentum \mathbf{K} or \mathbf{K}' , outgoing modes into which the incoming mode has been reflected at the boundary (expressed by the scattering matrix S), and evanescent modes, where S_{ev} gives the amplitudes to scatter into them, equivalently to S . With $\Psi_B = (\psi_{B,\mathbf{K}}, \psi_{B,\mathbf{K}'})$, where the additional subscript \mathbf{K}, \mathbf{K}' distinguishes the boundary wavefunctions depending on the momentum of the incoming modes, the last two blocks of the Schrödinger equation $H \begin{pmatrix} \Psi_L \\ \Psi_B \end{pmatrix} = 0$ yield

$$\begin{pmatrix} T_L \Psi_{\text{out}} & T_L \Psi_{\text{ev}} & -T_{LB} \\ T_{LB}^\dagger \Psi_{\text{out}} \Lambda_{\text{out}} & T_{LB}^\dagger \Psi_{\text{ev}} \Lambda_{\text{ev}} & H_B \end{pmatrix} \begin{pmatrix} S \\ S_{\text{ev}} \\ \Psi_B \end{pmatrix} = \begin{pmatrix} -T_L \Psi_{\text{in}} \\ -T_{LB}^\dagger \Psi_{\text{in}} \Lambda_{\text{in}} \end{pmatrix}. \quad (\text{S67})$$

We find that $T_L \Psi_{\text{ev}}^- = 0$, $T_{LB}^\dagger \Psi_{\text{ev}}^+ = 0$. Applying a discrete Fourier transform of both equation blocks by multiplying from the left by

$$\begin{pmatrix} U \otimes \mathbb{1}_4 & 0 \\ 0 & U \end{pmatrix}, \quad U_{mn} = \frac{1}{\sqrt{N}} e^{2\pi i(N-m)(N-n)/N} = \frac{1}{\sqrt{N}} e^{2\pi i m n / N}, \quad (\text{S68})$$

and explicitly computing all blocks of the system using the definitions given before, we get

$$\left(\begin{array}{cccc|c} 0 & 0 & 0 & 0 & \\ -A_2 & 0 & 0 & 0 & \\ 0 & 0 & 0 & \Lambda_{\text{ev}}^+ & \mathbb{1} + \Xi^\dagger \\ -A_1 & 0 & 0 & 0 & \\ 0 & 0 & 0 & 0 & \\ \hline 0 & 0 & \Xi_{\text{ev}}^{->} & 0 & \\ \alpha^* A_2 & 0 & 0 & 0 & \\ 0 & 0 & 0 & 0 & U H_B U^\dagger \\ -\alpha A_1 & 0 & 0 & 0 & \\ 0 & \Xi_{\text{ev}}^{-<} & 0 & 0 & \end{array} \right) \begin{pmatrix} S \\ S_{\text{ev}}^{-<} \\ S_{\text{ev}}^{->} \\ S_{\text{ev}}^+ \\ U \Psi_B \end{pmatrix} = \begin{pmatrix} 0 \\ A_1 \\ 0 \\ A_2 \\ 0 \\ 0 \\ \alpha^* A_1 \\ 0 \\ -\alpha A_2 \\ 0 \end{pmatrix}. \quad (\text{S69})$$

with

$$A_1 = \left(\frac{1}{\sqrt{2}}, 0 \right), \quad A_2 = \left(0, \frac{1}{\sqrt{2}} \right), \quad (\text{S70})$$

and

$$\begin{aligned} \Xi_{\text{ev}}^{-<} &= \text{diag}(\xi_{-\frac{N}{3}+1}, \dots, \xi_0), \quad \Xi_{\text{ev}}^{->} = \text{diag}(\xi_1, \dots, \xi_{\frac{N}{3}-1}), \quad \Xi_{\text{ev}}^- = \text{diag}(\Xi_{\text{ev}}^{-<}, \Xi_{\text{ev}}^{->}), \\ \Xi &= \text{diag}(\xi_1, \dots, \xi_N) = \text{diag}(\Xi_{\text{ev}}^{->}, \xi_{\mathbf{K}}, \Xi_{\text{ev}}^+, \xi_{\mathbf{K}'}, \Xi_{\text{ev}}^{-<}). \end{aligned} \quad (\text{S71})$$

Correspondingly, the evanescent modes scattering matrix S_{ev} is split up into parts for the same momentum ranges as $S_{\text{ev}} = (S_{\text{ev}}^{-<}, S_{\text{ev}}^{->}, S_{\text{ev}}^+)^T$. The lower right block of Eq. (S69) has the form

$$U H_B U^\dagger = \frac{1}{\sqrt{N}} \begin{pmatrix} \tilde{V}_0 & \tilde{V}_1 & \dots & \tilde{V}_{N-1} \\ \tilde{V}_1^* & \tilde{V}_0 & \ddots & \vdots \\ \vdots & \ddots & \ddots & \tilde{V}_1 \\ \tilde{V}_{N-1}^* & \dots & \tilde{V}_1^* & \tilde{V}_0 \end{pmatrix}, \quad (\text{S72})$$

with the Fourier coefficients of the disorder potential

$$\tilde{V}_k = \frac{1}{\sqrt{N}} \sum_{j=0}^{N-1} V_j e^{2\pi i(j-1)k/N}. \quad (\text{S73})$$

By clever pivoting, *i.e.*, exchanging the rows and columns of Eq. (S69), we can bring the system into a block-diagonal form where the lower right $((N/3 + 3) \times (N/3 + 3))$ -block does not depend on S_{ev} , thus leaving us with

$$\begin{pmatrix} \bar{V} & B_1 \\ C & D_1 \end{pmatrix} \begin{pmatrix} \bar{\Psi} \\ S \end{pmatrix} = \begin{pmatrix} B_2 \\ D_2 \end{pmatrix}. \quad (\text{S74})$$

Here $\bar{\Psi}$ contains some of the components of $U\Psi_B$ which however will be eliminated in the procedure of solving for S and therefore do not need to be specified. The matrix

$$\bar{V} = \frac{1}{\sqrt{N}} \left(\begin{array}{ccc|cc} \tilde{V}_0 & \dots & \tilde{V}_{\frac{N}{3}-2} & \tilde{V}_1^* & \tilde{V}_{\frac{N}{3}-1} \\ \vdots & \ddots & \vdots & \vdots & \vdots \\ \tilde{V}_{\frac{N}{3}-2}^* & \dots & \tilde{V}_0 & \tilde{V}_{\frac{N}{3}-1}^* & \tilde{V}_1 \\ \hline \tilde{V}_1 & \dots & \tilde{V}_{\frac{N}{3}-1} & \tilde{V}_0 & \tilde{V}_{\frac{N}{3}} \\ \tilde{V}_{\frac{N}{3}-1}^* & \dots & \tilde{V}_1^* & \tilde{V}_{\frac{N}{3}}^* & \tilde{V}_0 \end{array} \right) \quad (\text{S75})$$

contains only the lowest third of the Fourier components of the disorder potential V_j . Further, the remaining blocks of the system are given by

$$C = \begin{pmatrix} 0 & \dots & 0 \\ 0 & \dots & 0 \end{pmatrix} \begin{array}{c|c} 1 + \xi_{\mathbf{K}'} & 0 \\ \hline 0 & 1 + \xi_{\mathbf{K}} \end{array}, \quad B_1 = \begin{pmatrix} 0 & 0 \\ \vdots & \vdots \\ 0 & 0 \\ \hline 0 & \frac{\alpha^*}{\sqrt{2}} \\ \frac{-\alpha}{\sqrt{2}} & 0 \end{pmatrix}, \quad B_2 = \begin{pmatrix} 0 & 0 \\ \vdots & \vdots \\ 0 & 0 \\ \hline \frac{\alpha^*}{\sqrt{2}} & 0 \\ 0 & \frac{-\alpha}{\sqrt{2}} \end{pmatrix}, \quad D_1 = \begin{pmatrix} 0 & -\frac{1}{\sqrt{2}} \\ -\frac{1}{\sqrt{2}} & 0 \end{pmatrix}, \quad D_2 = \begin{pmatrix} \frac{1}{\sqrt{2}} & 0 \\ 0 & \frac{1}{\sqrt{2}} \end{pmatrix}. \quad (\text{S76})$$

Assuming the invertibility of \bar{V} and $D_1 - C\bar{V}^{-1}B_1$, we can use standard block matrix inversion to solve Eq. (S74) by multiplying with $\begin{pmatrix} \bar{V} & B_1 \\ C & D_1 \end{pmatrix}^{-1}$ from the left. We thereby obtain

$$S = [D_1 - C\bar{V}^{-1}B_1]^{-1} (D_2 - C\bar{V}^{-1}B_2), \quad (\text{S77})$$

reducing the problem to the inversion of \bar{V} . Due to the structure of B_1 , B_2 , and C , we only need to know the lower right 2×2 block of \bar{V}^{-1} , which we denote by

$$\bar{V}^{-1} = \begin{pmatrix} \ddots & & & & \\ & \ddots & & & \\ & & \ddots & & \\ \hline & & & W_{11} & W_{12} \\ & & & W_{21} & W_{22} \end{pmatrix}. \quad (\text{S78})$$

As \bar{V} (and therefore also W) is Hermitian, it must hold that $W_{11}, W_{22} \in \mathbb{R}$ and $W_{21} = W_{12}^*$. Further, from the structure of \bar{V} we conclude that $W_{11} = W_{22}$. We formally obtain $Y = W^{-1}$ by again using block matrix inversion. Y

is then given by the Schur complement of the upper left block of \bar{V} as

$$Y = \begin{pmatrix} Y_{11} & Y_{12} \\ Y_{12}^* & Y_{11} \end{pmatrix} = \frac{1}{\sqrt{N}} \left[\begin{pmatrix} \tilde{V}_0 & \tilde{V}_{\frac{N}{3}} \\ \tilde{V}_{\frac{N}{3}}^* & \tilde{V}_0 \end{pmatrix} - \begin{pmatrix} \tilde{V}_1 & \dots & \tilde{V}_{\frac{N}{3}-1} \\ \tilde{V}_{\frac{N}{3}-1}^* & \dots & \tilde{V}_1^* \end{pmatrix} \begin{pmatrix} \tilde{V}_0 & \dots & \tilde{V}_{\frac{N}{3}-2} \\ \vdots & \ddots & \vdots \\ \tilde{V}_{\frac{N}{3}-2}^* & \dots & \tilde{V}_0 \end{pmatrix}^{-1} \begin{pmatrix} \tilde{V}_1^* & \tilde{V}_{\frac{N}{3}-1} \\ \vdots & \vdots \\ \tilde{V}_{\frac{N}{3}-1}^* & \tilde{V}_1 \end{pmatrix} \right]. \quad (\text{S79})$$

From Eq. (S77) we can straightforwardly write down S in terms of the Y_{ij} , resulting in

$$S = \frac{1}{1 - \det Y + 2iY_{11}} \begin{pmatrix} 2\alpha Y_{12}^* & 1 + \det Y \\ 1 + \det Y & -2\alpha^* Y_{12} \end{pmatrix}. \quad (\text{S80})$$

The scattering phase ϕ can be obtained as

$$\phi = \arg(S_{12}) = \text{atan2}(1 - \det Y, -2Y_{11}). \quad (\text{S81})$$

4. Distribution of the scattering phase

Since the structure of the Y_{ij} is completely analogous to that of \tilde{m} in Eq. (S17), the same reasoning can be applied to distinguish whether or not the boundary overlaps with the band of edge states. When the edge states are shifted away from $E = 0$, *i.e.*, in the limit $s_d \ll V_d$, we obtain

$$\mathbb{E}[\phi] = -\arctan\left(\frac{2V_d}{1 - V_d^2}\right) + \frac{2}{3} \frac{s_d^2}{V_d(1 + V_d^2)} - \frac{a}{L} \cdot \frac{2(1 - V_d^2)}{V_d(1 + V_d^2)^2} s_d^2 + \mathcal{O}\left(\frac{s_d^3}{V_d^3}\right), \quad (\text{S82})$$

$$\text{Var}(\phi) = \frac{a}{L} \frac{4s_d^2}{(1 + V_d^2)^2} + \mathcal{O}\left(\frac{s_d^3}{V_d^3}\right). \quad (\text{S83})$$

For a boundary with $V_d = 0$ that fulfills the condition of diffusive scattering, we can again not solve for ϕ as a function of L . We can however compute an explicit expression for $L = 6$,

$$\mathbb{E}[\phi_6] = 0, \quad \text{Var}(\phi_6) = \sqrt{\frac{4\pi}{3}} \ln(2) s_d + \mathcal{O}(s_d^2) \approx 1.4 s_d, \quad (\text{S84})$$

which we find numerically to be in good agreement with the results for larger L .

C. Comparison between Dirac equation and tight-binding model

The results obtained from the Dirac equation and the tight-binding model show qualitative agreement for both broken and preserved law of reflection. To also find a quantitative relation, we compare Eq. (S31) to Eq. (S83) and Eq. (S36) to Eq. (S84). To equate the results of the two models for both cases, we have to assume that the scattering phases in the two models are not the same (due to the different number of modes), but related by some factor, $\text{Var}_{\text{tb}}(\phi) \propto \text{Var}_{\text{Dirac}}(\phi)$. Also assuming $s_d \propto s_\theta$, we find $\text{Var}_{\text{tb}}(\phi) \simeq 0.1 \text{Var}_{\text{Dirac}}(\phi)$ and $s_d \simeq 0.1 s_\theta$.

D. Magnetic focusing conductance in the absence of edge disorder

In order to verify that the conductance dip at the second focusing resonance is a consequence of edge disorder, we compare the focusing conductance with edge disorder to the focusing conductance of a device with a clean boundary. The setup is otherwise the same as the one we present in the main text, with the parameters identical to those used to obtain Figs. 3 (b)-(d) of the main text.

The results are shown in Fig. S3, where Fig. S3 (a) shows the focusing conductance versus gate voltage and magnetic field strength without disorder, *i.e.*, with $V_d = s_d = 0$. The average potential at the boundary aligns with the Fermi level at a gate voltage $V_G \approx 0.2$ eV, which is larger than in the case with disorder included (see also Fig. 3 (b) of the main text). This distinction arises due to the difference in the average edge disorder potential V_d , which is nonzero when disorder is included. At large negative gate potentials $V_G \lesssim -0.15$ eV, resonant conductance oscillations also

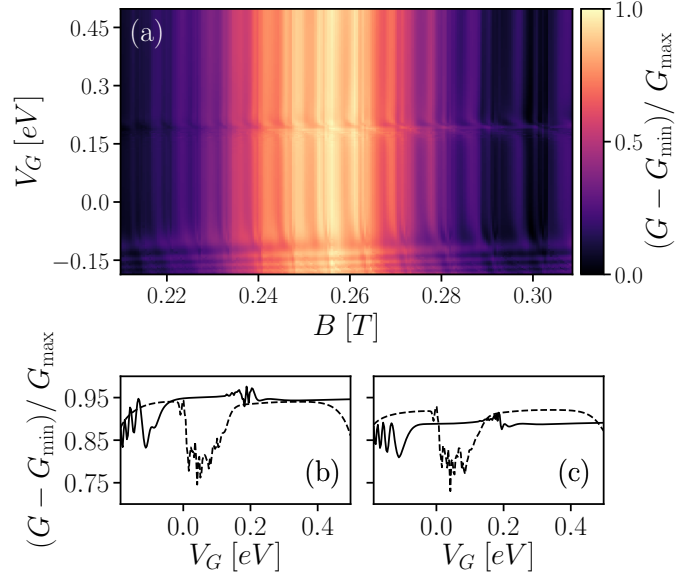


FIG. S3. (a) Conductance around the second focusing peak at $E_F = 0.093$ eV versus gate voltage without edge disorder, *i.e.*, $V_d = s_d = 0$. (b) Line cuts of the focusing conductance at $B = 0.255$ T versus gate voltage, without edge disorder (solid line) from (a), and with edge disorder from Fig. 3 (b) of the main text (dashed line). (c) Line cuts of the focusing conductance versus gate voltage averaged over the magnetic field values $0.247 \leq B \leq 0.259$ T at the second focusing resonance, without (solid line) and with (dashed line) edge disorder. The data with disorder is taken from Fig. 3 (b) of the main text. In the absence of edge disorder, a small region of resonant conductance peaks appears around $V_G = 0.2$ eV, as the average potential in the boundary aligns with the Fermi level, but unlike the case with disorder, no clear dip is present. When the boundary is clean, the gate forms a quantum well by the boundary at large negative gate potentials $V_G \lesssim -0.15$ eV, resulting in resonant oscillations in the conductance. Similar oscillations also appear in the case with edge disorder, but at even larger negative gate potentials because of an overall average potential shift by the boundary due to onsite disorder, $V_d = 0.062$ eV.

appear because the gate forms a quantum well by the boundary. A similar phenomenon occurs in the case with edge disorder, but outside the energy window we consider, and is unrelated to the mechanism we are investigating. In Fig. S3 (a), some conductance oscillations appear in the conductance around the charge neutrality point $V_G \approx 0.2$ eV, but no clear dip is visible. Furthermore, Fig. S3 (b) gives a comparison of conductance line cuts at $B = 0.255$ T for a clean boundary with the case including edge disorder from Fig. 3 (b) of the main text. We see that the oscillations when the edge potential aligns with the Fermi level in the clean case are much smaller in scale than the conductance dip that appears with the inclusion of edge disorder. The same trends are visible in Fig. S3 (c), which compares the focusing conductance averaged over magnetic field values at the second focusing peak, with and without edge disorder. Therefore, we conclude that the dip in the focusing conductance at the second focusing peak arises due to edge disorder, namely when the average potential at the boundary aligns the disordered band of edge states with the Fermi level.